Physics of Double Faceted Crystal Growth in Solidification Processes

Alireza Pirnia[a], Brian T. Helenbrook[a,*]

[a]*Department of Mechanical and Aeronautical Engineering, Clarkson University, 8 Clarkson Ave., Box 5725, Potsdam, NY 13699, USA*

Abstract

The existence of solidification growth fronts having intersecting facets (double faceted) has recently been observed in silicon experiments of horizontal ribbon growth. This study investigates the physics of such configurations from a continuum perspective by analyzing the variation of temperature at locations where a facet intersects another facet or a free surface. The temperature distribution and gradients are obtained theoretically for different configurations and material properties. The theoretical formulations show that the intersection point of two facets is colder than the surrounding interface temperatures and thus could be a nucleation site. The analysis also shows that there is a supercooled liquid (below the interface temperatures) in front of the intersection point. However, this is only the case for materials that have a solid conductivity less than the liquid conductivity such as silicon. It is also shown, to the extent that continuum assumptions remain valid, that the temperature gradients can approach infinity at either the intersection point between two facets or the intersection of a facet with a free surface, depending on the material properties and configurations. The theoretical predictions in the vicinity of these points are validated using a finite element numerical solution that accounts for thermal transport, liquid convection, and solidification kinetics. This shows that the physical behavior of a double facet formation can be theoretically predicted informing further experimental, continuum numerical, and molecular dynamic investigations of the phenomenon.

Keywords: A1. Interfaces, A1.Facets, A1. Heat transfer, A1. Physics of solidification, B2. Semiconducting silicon, B3. Solar cells

1. Introduction

Formation of facets is common in the growth of oxides and semiconductors [1]. They have been observed in different crystallization processes such as Czochralski (CZ) [2–4], floating zone (FZ) [5], and horizontal ribbon growth (HRG) [6–8]. Facets can have implications for the solidified product such as stress concentrations and dopant segregation [4, 9]. In the Czhochralski process in particular, facets are known to be one of the causes for spiral growth [1]. As such, they have been studied extensively in the past to understand their nature and the conditions leading to their formation.

Faceted crystal growth occurs on low-index surfaces that have a low free surface energy [9]. In the specific case of crystallized silicon, the criterion proposed by Jackson [10] predicts that only facets formed on a {111} plane are atomically smooth and all other surfaces are rough. Formation of facets on the solid-liquid interface is accompanied by a local reduction in interface temperature below the equilibrium melting point, referred to as supercooling or undercooling. This temperature reduction is attributed to anisotropy in interfacial energy or attachment kinetics [11]. Facet kinetics consists of nonlinear step sources and subsequent linear propagation of steps across the facet. Dislocations and 2D nucleation of atoms at the solid-liquid interface are two general types of step sources [12]. While growth of the solid-liquid interface is in general a function of local temperature gradients, the evolution of facets is a function of solidification kinetics as well, and therefore, their analysis requires a knowledge of appropriate kinetic models [13].

Kinetic models are often expressed as $u_{\mathrm{I,g,n}} = \Delta T_{\mathrm{I}}/K$, where $u_{\mathrm{I,g,n}}$ is the normal interface growth rate, ΔT_{I} is the local interface supercooling, and K is the kinetic coefficient. In the kinetics model proposed by Weinstein and Brandon [14], the kinetic coefficient is an exponential function of ΔT_{I} for 2D nucleation and a quadratic function of ΔT_{I} for dislocations. It has been shown that 2D nucleation of atoms requires substantial liquid supercooling and its growth rate is slow [15]. The kinetic

*Corresponding author

Email address: bhelenbr@clarkson.edu (Brian T. Helenbrook)

coefficient for subsequent step growth on the facet is a function of local interface curvature and varies with the inverse of the interface misalignment angle, *i.e.*, the angle between local interface normal and facet face normal. At larger misalignment angles, the liquid-solid interface deviates from a facet and roughly aligns with the melting point isotherm with roughened growth and a constant kinetic coefficient [14]. It should be noted, however, that such models are obtained for single isolated facets formed on a solid-liquid interface and may not hold for other configurations that might have different physics. Formation of twin facets on parallel grain boundaries [16–18], facets formed inside the grooves between grain boundaries [19, 20], and faceted dendritic growth [21–23] are examples of such configurations.

Configurations of interest in this paper are where a single facet intersects a free surface at a triple junction point (TJP), where the solid, liquid, and gas phases meet, or where a facet intersects another growth facet, such as a (111) intersecting a ($\underline{1}$11) facet, at a point submerged in the liquid. The intersection point is referred to herein as a double facet point (DFP) and the configuration is referred to as a double facet formation. Such formation occurs during the CZ and FZ processes, where ridges have been sometimes observed around the perimeter of solidified boules [5, 24, 25]. In the experimental study of the HRG technique by Kellerman et al. [26], a ($\underline{1}$11) and (111) double facet formation was observed under the liquid surface (see Fig. 1) and it was assumed that the facet intersection point was the step source for the two facets. Single facets were also observed to intersect the free surface at a TJP.

The facet configuration can significantly change the physics of the problem because of the different heat flux profiles around the two points. As such, it is imperative to study the physics of the solidification process at both point types to better understand the mechanisms of a double facet formation. This study performs a detailed theoretical and numerical analysis in the vicinity of a double facet formation, an investigation that has never been done before. An HRG configuration is chosen as the backdrop for this study because both a facet TJP and s DFP exist in this configuration. However, the general analysis can be extended to other double facet configurations as well. The objectives of this study is to examine the physics of a double facet formation as a function of temperature variations and the interactions with the solidification kinetics in the vicinity of the double facet. Results of this analysis provide valuable information about the nature of such phenomena, leading to a more informed prediction of the performance and stability of solidification processes in the presence of a double facet configurations.

2. Problem Description

Figure 1(a) shows a schematic of the HRG technique for crystal growth with a double facet formation at the crystal leading edge (LE), denoted by a dashed circle. In the HRG technique, an initial crystal seed is placed on the free surface of a molten pool (Ω_l) inside a crucible with depth d, and a cooling jet of a non-reacting gas (such as Helium) is blown on the pool surface. The seed grows and a solidified single-crystal ribbon (Ω_s) is formed that floats on the liquid if the solid density is smaller than the liquid. Silicon is an example of such material. The ribbon (sheet) is continuously pulled out of the pool with a pulling speed vector $\vec{u}_\mathrm{p}$ and is cut to size. As long as the rate of solidified material extraction equals the ribbon growth rate and no destabilizing phenomenon occurs, a steady-state process can be maintained such that the ribbon LE seems to be stationary from an observer's perspective [27]. It is assumed here that the solidification process in the HRG technique is mainly uniform across the span (normal to page) of the ribbon and three-dimensional edge effects are negligible. Therefore, the problem is studied at a cross-section of the crucible in the middle of its span.

An enlarged view of the double facet formation at the ribbon LE is shown in Fig. 1(b) with the chosen coordinate system. The solid-gas and liquid-gas interfaces and the pulling speed vector are assumed to align with the x-axis (horizontal), such that $\vec{u}_\mathrm{p} = u_\mathrm{p}\hat{x}$. The top surface of the seed is aligned with the (100) plane and the growth direction is [011]. The cooling heat flux from the liquid-gas and solid-gas interfaces is denoted by $q_\mathrm{l}(x)$ and $q_\mathrm{s}(x)$, respectively. The heat fluxes consist of convective and radiative heat transfer and may be discontinuous at the TJP due to a possible difference in liquid and solid emissivities. The solid-liquid interface makes an angle of θ_TJP with the $-x$ direction at the TJP. The double facet consists of ($\underline{1}$11) and (111) facets, referred to herein as the top and bottom facets, respectively. The facet intersection point is a DFP, at which the angles of the two facets with the x-axis are $\theta_\mathrm{DFP,t}$ and $\theta_\mathrm{DFP,b}$, respectively. This configuration is consistent with the experimental observations by Kellerman et al. [26], as shown in Fig. 1(c). This picture was obtained by an antimony demarcation method of an HRG experiment where a roughly 1 [mm] thick sheet was pulled from a pool of a depth of 13 [mm] at a rate of 0.5 [mm/s]. It clearly shows the formation of top and bottom facets that are aligned with ($\underline{1}$11) plane with $\pi - \theta_\mathrm{f}$ angle and (111) plane with θ_f angle from the x-axis, respectively,

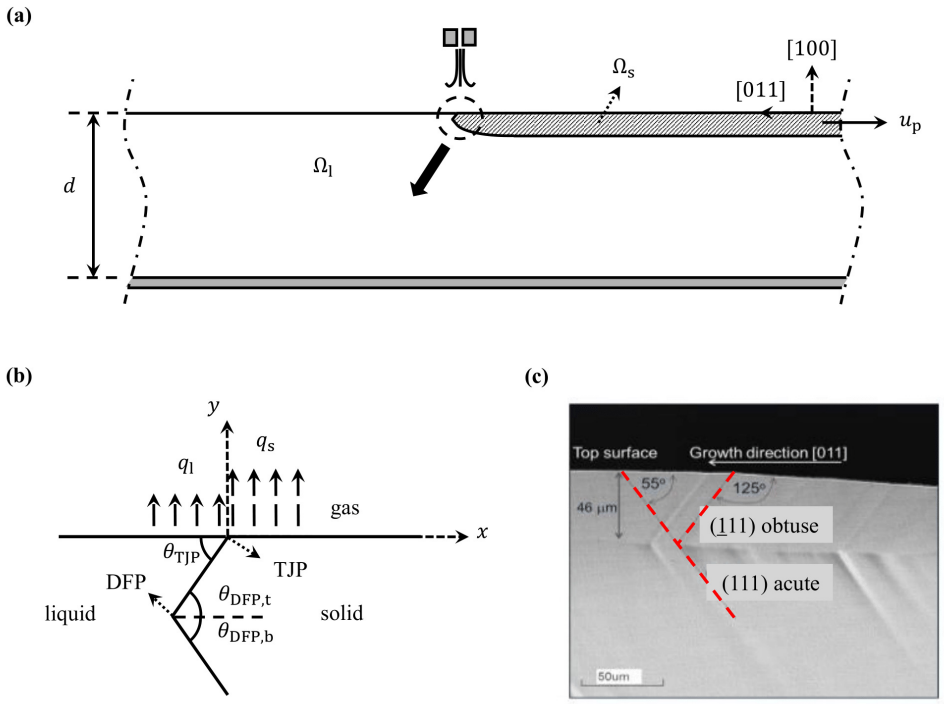

Figure 1: Cross-section view of a solidified ribbon in the HRG process with a double facet formation at its LE, with (a) schematic of the orientation of liquid (Ω_l) and solid (Ω_s) domains with respect to the pulling speed direction, (b) close view of the double facet showing ($\underline{1}11$) (upper) and (111) (lower) facets, TJP and DFP, and the respective angles, (c) double facet formation and orientations observed in an HRG experiment, opted from Kellerman et al. [26].

where $\theta_f \approx 55^\circ$ is the angle that a (111) facet makes with the x-axis and is referred to herein as the facet angle.

Because there is little information from the experimental observations regarding the exact shape of the double facet and the temperature variations in its vicinity, a few assumptions and simplifications are made in this study. Based on the experimental observation that the DFP is the leading propagation point on the solid-liquid interface, it is assumed that the DFP is the initiation point of steps that propagate outward on both the top and bottom facets. Thus, nucleation is assumed to occur at the DFP. For this analysis, the top and bottom facet angles are assumed equal ($\theta_{DFP,t} = \theta_{DFP,b}$), such that the problem is geometrically symmetric around the DFP. Furthermore, it is assumed that the problem is also thermally symmetric around the DFP. This means that the heat flux in the y-direction is assumed zero along a horizontal line (in x-direction) passing through the DFP (see Fig. 2). With this simplification, the problem only needs to be studied on the top facet where both DFP and TJP exist. While the thermal symmetry assumption is not true for all scenarios, it is accurate for some configurations, and may be a good assumption local to the DFP.

3. Theoretical Model

In this section, the problem is studied theoretically in the vicinity of the two points of interest, the TJP and DFP. A schematic of the two points and the coordinate systems used for their study is shown in Fig. 2, where x^* is aligned with the facet tangent and y^* with the facet normal, r is the distance from each point, and θ is the angle of deviation from the facet direction in the counter-clockwise direction. At the TJP (or DFP), the angles of the liquid-gas (or liquid-liquid) and solid-gas (or solid-solid) interfaces in their respective coordinate system are θ_l and θ_s, respectively, which may be positive or negative depending on the case.

Following the same discussion as in [7] and [8], the heat balance equation in the vicinity of each point reduces to $\nabla^2 T_i = 0$ in the $r < \epsilon$ limit, where subscript i refers to either the liquid, l, or solid, s, domains. For this equation to be valid, the radius of investigation (ϵ)

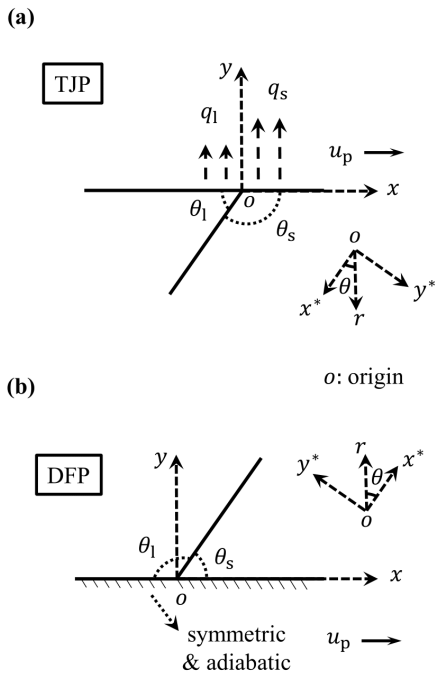

Figure 2: Schematic of the top facet of a double facet formation in the vicinity of (a) the TJP and (b) the DFP and the coordinate systems used for the analysis of the problem. The double facet is assumed geometrically and thermally symmetric about the x-axis at the DFP.

should be small such that the convective terms can be assumed negligible provided that the Peclet number is small, i.*e*., $\mathrm{Pe_i} = \rho_i c_i u_p \epsilon / k_i << 1$, where ρ_i, c_i, and k_i are the density, specific heat, and thermal conductivity of each domain [8]. In the small circle close to the TJP, the cooling heat fluxes from the solid and liquid domains can be assumed constant at values of q_s and q_l, respectively. These two values are not usually equal in the presence of radiation due to unequal liquid and solid emissivities. The heat flux normal to the symmetry line at the DFP is zero.

For the TJP (or DFP) in Fig. 2, the known boundary conditions for the solution of the heat balance equation are: (1) constant heat flux at the liquid-gas (or liquid-liquid) interface, $\theta = \theta_l$, with $-k_l \nabla T_l \cdot \hat{n}_l = q_l$, (2) constant heat flux at the solid-gas (or solid-solid) interface, $\theta = \theta_s$ with $-k_s \nabla T_s \cdot \hat{n}_s = q_s$, (3) equal temperatures at the solid-liquid interface, $\theta = 0$, with $T_l = T_s$, (4) heat release due to solidification at the solid-liquid interface with $-k_s \nabla T_s \cdot \hat{n}_s - k_l \nabla T_l \cdot \hat{n}_l = \rho_s L_f \vec{u}_p \cdot \hat{n}_s$, and (5) finite temperature at $r = 0$, where L_f is the latent heat of fusion and $\hat{n}_l$ and $\hat{n}_s$ are the normals to the liquid and solid domains, respectively, at each interface. Note that the heat fluxes are assumed zero at the DFP, $q_{l,\mathrm{DFP}} = q_{s,\mathrm{DFP}} = 0$. Because of non-homogeneous boundary conditions (1), (2), and (4), the solution for this problem at each point and each domain can be assumed as the superposition of a non-homogeneous, $T_{i,nh}$, and a homogeneous, $T_{i,h}$, solution.

For the non-homogeneous solution, a linear formula can be assumed because of constant heat fluxes at the free surfaces at the TJP and zero heat fluxes at the symmetry line at the DFP, such that

$$\begin{aligned} T_{i,nh}(x^*, y^*) &= T(r=0) + \frac{\partial T_{i,nh}}{\partial x^*} x^* + \frac{\partial T_{i,nh}}{\partial y^*} y^* \\ &= T(r=0) + A_i x^* + B_i y^*, \end{aligned} \tag{1}$$

where $T(r = 0)$ is the temperature at $r = 0$, and A_i and B_i are constants for the liquid and solid domains (i = l or s). To satisfy the third boundary condition at the solid-liquid interface (temperature continuity), $A_l = A_s = A$ for both points. The solutions for A and B_i at each point are obtained in §4. With the assumptions of this problem, $T(r = 0)$ is unknown. However if either points are a source of step nucleation, $T(r = 0)$ can be implicitly obtained from the solidification kinetic formulations, as will be shown in §5.

The boundary conditions for the homogeneous solution at both points become: (1) $-k_l \nabla T_{l,h} \cdot \hat{n}_l = 0$ at $\theta = \theta_l$, (2) $-k_s \nabla T_{s,h} \cdot \hat{n}_s = 0$ at $\theta = \theta_s$, (3) $T_{l,h} = T_{s,h}$ at $\theta = 0$, (4) $-k_s \nabla T_{s,h} \cdot \hat{n}_s - k_l \nabla T_{l,h} \cdot \hat{n}_l = 0$ at $\theta = 0$, and (5) zero temperature at $r = 0$. With these boundary conditions, the homogeneous solution can be obtained in the r-θ plane by the method of separation of variables in the form of $T_{i,h}(r, \theta) = \psi_i(\theta)\eta_i(r)$. Plugging this definition for temperature into the governing equation results in a set of solutions of $\psi_i(\theta) = C_i \cos(\lambda\theta) + D_i \sin(\lambda\theta)$ and $\eta_i(r) = E_i r^{\lambda} + F_i r^{-\lambda}$ (i = l or s), where λ and the coefficients are constants that need to be determined based on the boundary conditions.

Assuming $\lambda > 0$, the fifth boundary condition (finite temperature) results in $F_i = 0$. Therefore the solution can be presented as $T_{i,h} = (G_i \cos(\lambda\theta) + H_i \sin(\lambda\theta)) r^{\lambda}$. Satisfying the other boundary conditions leads to a system of equations in the form of $\mathrm{M}\boldsymbol{g} = 0$, where M is a 4×4 matrix and $\boldsymbol{g}$ is the vector of solution constants. For a non-trivial solution, the determinant of M must be zero:

$$\frac{k_s - k_l}{2} \sin(\lambda(\theta_l + \theta_s)) - \frac{k_s + k_l}{2} \sin(\lambda(\theta_l - \theta_s)) = 0. \tag{2}$$

Solving this equation results in infinite series of solutions for λ_n ($n = 1 \rightarrow \infty$) that are a function of the thermal conductivities of the material of interest and the angles that the liquid-gas interface at the TJP (or liquid-liquid at the DFP) and solid-gas interface at the TJP (or

solid-solid at the DFP) make with the local facet. Note that for the special case shown in Fig. 2 where both the gas interfaces at the TJP (or symmetry interfaces at the DFP) are horizontal, Eq. (2) is simplified because $\theta_\mathrm{l} + \theta_\mathrm{s} = \pi - 2\theta_\mathrm{tj}$ at the TJP (or $\pi - 2\theta_\mathrm{f}$ at the DFP) and $\theta_\mathrm{l} - \theta_\mathrm{s} = -\pi$ at the TJP (or π at the DFP).

With the obtained λ_n, the homogeneous solution in the liquid and solid domains for both the TJP and DFP can be re-written as

$$T_{\mathrm{i,h}}(r,\theta) = \sum_{n=1}^{\infty} \frac{G_\mathrm{n}}{\cos(\lambda_\mathrm{n}\theta_\mathrm{i})} \cos(\lambda_\mathrm{n}(\theta - \theta_\mathrm{i}))\, r^{\lambda_\mathrm{n}}, \quad (3)$$

where $G_\mathrm{n} = G_{\mathrm{l,n}} = G_{\mathrm{s,n}}$ based on the third boundary condition (temperature continuity). The G_n coefficients are unknown and should be obtained from a boundary condition on a finite radius arc surrounding each point. Because it is assumed that $\lambda_\mathrm{n} > 0$, the homogeneous solution of Eq. (3) approaches zero at all λ_n as $r \to 0$ close to both points. Consequently, the temperature distribution in the vicinity of each point is determined by the non-homogeneous solution. In other words, the leading order term of the solution dominates as $r \to 0$. It should be noted, however, that this may not be true for the homogeneous temperature gradients, $\partial T_{\mathrm{i,h}}/\partial r$ and $(1/r)\partial T_{\mathrm{i,h}}/\partial\theta$, because the gradients will approach infinity for $0 < \lambda_\mathrm{n} < 1$ and therefore they should not be ignored in such conditions.

The temperature gradients at the TJP and DFP can have a significant influence on the stability of crystal formation. After the temperature distributions are obtained, the temperature gradients in the tangential, x^*, normal, y^*, horizontal, x, and vertical, y, directions can be computed as

$$\begin{aligned}
\frac{\partial T_\mathrm{i}}{\partial x^*} &= \left(\frac{\partial T_{\mathrm{i,h}}}{\partial r}\right)_{\theta=0} + \frac{\partial T_{\mathrm{i,nh}}}{\partial x^*},\\
\frac{\partial T_\mathrm{i}}{\partial y^*} &= \frac{1}{r}\left(\frac{\partial T_{\mathrm{i,h}}}{\partial \theta}\right)_{\theta=0} + \frac{\partial T_{\mathrm{i,nh}}}{\partial y^*},\\
\frac{\partial T_\mathrm{i}}{\partial x} &= -\frac{\partial T_\mathrm{i}}{\partial x^*}\cos(\theta_\mathrm{l}) + \frac{\partial T_\mathrm{i}}{\partial y^*}\sin(\theta_\mathrm{l}),\\
\frac{\partial T_\mathrm{i}}{\partial y} &= -\frac{\partial T_\mathrm{i}}{\partial x^*}\sin(\theta_\mathrm{l}) - \frac{\partial T_\mathrm{i}}{\partial y^*}\cos(\theta_\mathrm{l}).
\end{aligned} \quad (4)$$

4. Discussion of the Theoretical Model

In this section, the application of the theoretical model at the two points of interest is described and the implications associated with different configurations and conditions are discussed.

4.1. Theoretical Prediction at the TJP

At the TJP in Fig. 2(a), the gas interface angles are $\theta_\mathrm{l} = -\theta_\mathrm{tj}$ and $\theta_\mathrm{s} = \pi - \theta_\mathrm{tj}$ and the free surface heat fluxes are constant values of q_l and q_s, respectively. The non-homogeneous solution in the vicinity of the TJP is obtained as

$$\begin{aligned}
T_\mathrm{i}(x^*, y^*) \approx T_\mathrm{TJP} &+ \left(-\frac{\rho_\mathrm{s} L_\mathrm{f} u_\mathrm{p}}{k_\mathrm{l} - k_\mathrm{s}}\cos(\theta_\mathrm{l}) + \frac{q_\mathrm{s} - q_\mathrm{l}}{k_\mathrm{l} - k_\mathrm{s}}\frac{1}{\sin(\theta_\mathrm{l})}\right) x^*\\
&+ \left(-\frac{\rho_\mathrm{s} L_\mathrm{f} u_\mathrm{p}}{k_\mathrm{l} - k_\mathrm{s}}\sin(\theta_\mathrm{l}) + \frac{q_\mathrm{s} - q_\mathrm{l}}{k_\mathrm{l} - k_\mathrm{s}}\frac{1}{\cos(\theta_\mathrm{l})} + \frac{q_\mathrm{i}}{k_\mathrm{i}}\frac{1}{\cos(\theta_\mathrm{l})}\right) y^*,
\end{aligned} \quad (5)$$

where the temperature at the TJP location, $T_\mathrm{TJP} = T(r = 0)$, is unknown. Whether the homogeneous temperature gradients can be ignored at the TJP depends on the specific configuration and the thermal conductivities of the material. Considering only the first term of the homogeneous solution, the tangential and normal temperature gradients in the vicinity of the TJP are stated as

$$\begin{aligned}
\frac{\partial T_\mathrm{l}}{\partial x^*} =& \frac{\partial T_\mathrm{s}}{\partial x^*} = -\frac{\rho_\mathrm{s} L_\mathrm{f} u_\mathrm{p}}{k_\mathrm{l} - k_\mathrm{s}}\cos(\theta_\mathrm{l}) + \frac{q_\mathrm{s} - q_\mathrm{l}}{k_\mathrm{l} - k_\mathrm{s}}\frac{1}{\sin(\theta_\mathrm{l})}\\
&+ G_1 r^{\lambda_1 - 1},\\
\frac{\partial T_\mathrm{l}}{\partial y^*} =& -\frac{\rho_\mathrm{s} L_\mathrm{f} u_\mathrm{p}}{k_\mathrm{l} - k_\mathrm{s}}\sin(\theta_\mathrm{l}) + \frac{q_\mathrm{s} - q_\mathrm{l}}{k_\mathrm{l} - k_\mathrm{s}}\frac{1}{\cos(\theta_\mathrm{l})} + \frac{q_\mathrm{l}}{k_\mathrm{l}}\frac{1}{\cos(\theta_\mathrm{l})}\\
&+ \lambda_1 G_1 \tan(\lambda_1\theta_\mathrm{l}) r^{\lambda_1 - 1},\\
\frac{\partial T_\mathrm{s}}{\partial y^*} =& -\frac{\rho_\mathrm{s} L_\mathrm{f} u_\mathrm{p}}{k_\mathrm{l} - k_\mathrm{s}}\sin(\theta_\mathrm{l}) + \frac{q_\mathrm{s} - q_\mathrm{l}}{k_\mathrm{l} - k_\mathrm{s}}\frac{1}{\cos(\theta_\mathrm{l})} + \frac{q_\mathrm{s}}{k_\mathrm{s}}\frac{1}{\cos(\theta_\mathrm{l})}\\
&+ \lambda_1 G_1 \tan(\lambda_1(\pi + \theta_\mathrm{l})) r^{\lambda_1 - 1}.
\end{aligned} \quad (6)$$

If $\lambda_1 < 1$, both tangential and normal gradients approach infinity as $r \to 0$. Assuming the misalignment angle at the TJP is small compared to the facet angle such that $\theta_\mathrm{l} \approx -\theta_\mathrm{f}$, and considering silicon as the crystallized material with $k_\mathrm{l} = 64\,[\mathrm{W/(m \cdot K)}]$ and $k_\mathrm{s} = 22\,[\mathrm{W/(m \cdot K)}]$ [28], the solutions of Eq. (2) at the TJP are $\lambda_1 = 0.8606$, $\lambda_2 = 2.088$, ... Thus, the model predicts that silicon will have infinite temperature gradients in this solidification configuration. It should be noted, however, that the continuum assumptions are no longer valid at very small radii (atomic scale), and therefore Eq. (6) is only valid to an extent close to the TJP.

An infinite temperature gradient can have implications for the stability of solidification processes. For example, the surface tension of liquid silicon is a strong function of the surface temperature gradient [29]. For the geometry shown in Fig. 2(a), the liquid free surface is aligned with the horizontal (x) direction. Combining Eq. (4) and (6), it can be concluded that the horizontal liquid temperature gradient at the TJP, $\partial T_\mathrm{l}/\partial x$, will also approach infinity if $\lambda_1 < 1$. This means there will be a large difference in liquid surface tension between the

TJP and the far-field, resulting in a large Marangoni-induced liquid flow in the vicinity of the TJP that may cause flow instability in the liquid pool [30, 31].

If we only examine the non-homogeneous solution, the temperature gradients are finite. For silicon, $q_s > q_l$ because the solid emissivity is greater than the liquid's. This implies that the tangential and normal gradients are always negative and positive, respectively. A negative tangential temperature gradient at the TJP means that the temperature decreases moving away from the TJP along the facet (see Fig. 2(a)), and therefore, the TJP is warmer than other locations on the facet in its vicinity, implying that it is probably not a source of crystal nucleation. However because $\lambda_1 < 1$, no conclusion can really be made regarding the sign of the temperature gradients at the TJP because the sign and value of G_1 is unknown.

Figure 3 explores the possibility of infinite temperature gradients at the TJP for various systems by plotting the first radial power of the homogeneous solution, λ_1, at varying liquid interface angles (see Fig. 2(a)) in different materials. More specifically, the plots are shown for materials with $k_l > k_s$ and materials with $k_l < k_s$, where silicon and yttrium aluminum garnet (YAG) properties are used, respectively [14]. It can be observed that the two material types have opposite behaviors. Note that the conditions mentioned above for a double facet in silicon with $\lambda_1 = 0.8606$ and infinite temperature gradients occur at $\theta_l = -0.31\pi$. At this facet angle, materials with $k_l < k_s$ will have finite temperature gradients at the TJP of a double facet formation.

At $\theta_l = -\pi/2$, the facet is vertical (normal to the free surface) with finite and constant homogeneous temperature gradients for both types of materials. Such a condition occurs at solidification near an adiabatic solid wall or in droplet solidification [7]. $\theta_l = -0.69\pi$ corresponds to the {111} acute facet shown in Fig. 1(c) extending to the free surface, where materials with $k_l > k_s$ (like silicon) would have a finite temperature gradients and materials with $k_l < k_s$ (like YAG) would have infinite gradients. At this angle, Eq. (6) predicts a finite and positive tangential temperature gradient for silicon, meaning that the TJP is a local temperature minima where crystal nucleation can occur. This situation was analyzed for silicon in prior work [8].

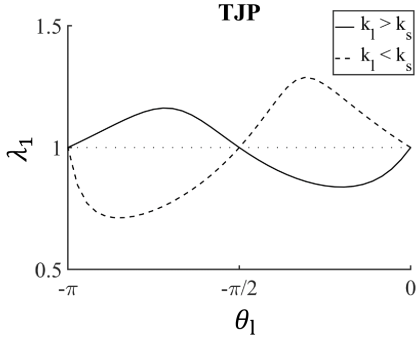

Figure 3: Variation of the first radial power of the homogeneous solution as a function of the liquid interface angle at the TJP for materials with $k_l > k_s$ and $k_l < k_s$.

4.2. Theoretical Prediction at the DFP

At the DFP in the coordinate system shown in Fig. 2(b), the misalignment angle is assumed small, such that the angles of the liquid-liquid and solid-solid interfaces are $\theta_l = \pi - \theta_f$ and $\theta_s = -\theta_f$, respectively. Also, the heat fluxes are zero because of the adiabatic boundary condition. The non-homogeneous temperature distribution in the vicinity of the DFP is obtained as

$$T_l(x^*, y^*) = T_s(x^*, y^*) \approx T_{DFP} + \left(-\frac{\rho_s L_f u_p}{k_l - k_s}\cos(\theta_l)\right) x^* + \left(-\frac{\rho_s L_f u_p}{k_l - k_s}\sin(\theta_l)\right) y^*, \tag{7}$$

where $T_{DFP} = T(r = 0)$ is the unknown temperature at the DFP location. Including the first term of the homogeneous solution, the tangential and normal temperature gradients at the DFP are equal to

$$\begin{aligned} \frac{\partial T_l}{\partial x^*} &= \frac{\partial T_s}{\partial x^*} = -\frac{\rho_s L_f u_p}{k_l - k_s}\cos(\theta_l) + G_1 r^{\lambda_1 - 1}, \\ \frac{\partial T_l}{\partial y^*} &= -\frac{\rho_s L_f u_p}{k_l - k_s}\sin(\theta_l) + \lambda_1 G_1 \tan(\lambda_1 \theta_l) r^{\lambda_1 - 1}, \\ \frac{\partial T_s}{\partial y^*} &= -\frac{\rho_s L_f u_p}{k_l - k_s}\sin(\theta_l) - \lambda_1 G_1 \tan(\lambda_1 (\pi - \theta_l)) r^{\lambda_1 - 1}. \end{aligned} \tag{8}$$

Similar to Fig. 3, the variation of λ_1 as a function of the liquid interface angle at the DFP (see Fig. 2(b)) is shown in Fig. 4 for the two types of materials. Comparing to Fig. 3, It is observed that the DFP behavior is opposite that of the TJP for the two material types. Considering silicon as the crystallized material ($k_l > k_s$) and $\theta_l = \pi - \theta_f = 0.69\pi$, as shown in Fig. 2(b), the solutions of Eq. (2) at the DFP are $\lambda_1 = 1.161$, $\lambda_2 = 1.882$, ..., indicating that the temperature gradients are finite at the DFP of a double {111} facet formation and are determined by the non-homogeneous solution. For materials with $k_l < k_s$, however, the DFP of a double {111} facet will have infinite temperature gradients according to Eq. (8).

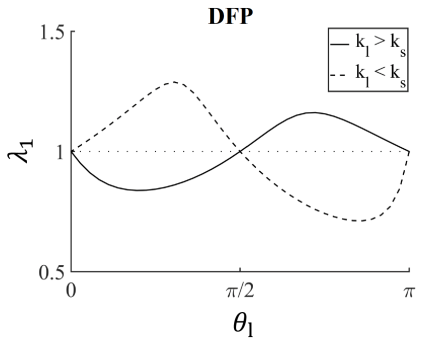

Figure 4: Variation of the first radial power of the homogeneous solution as a function of the liquid interface angle at the DFP for materials with $k_l > k_s$ and $k_l < k_s$.

For materials like silicon with $k_l > k_s$, the tangential temperature gradient is positive at the DFP, meaning the temperature locally increases by moving away from the DFP (positive x^* in Fig. 2(b)) on both the top and bottom facets (due to symmetry), making the DFP a local temperature minima and a potential point of step nucleation. The temperature at this point, T_{DFP}, must be such that the nucleation rate is consistent with the growth rate. As the kinetics of nucleation at such a point are unknown, it is impossible to determine T_{DFP}.

The normal temperature gradient is equal for both the solid and liquid domains, implying that the jump in heat flux to support the solidification is created by the jump in thermal conductivity. Furthermore, combining Eq. (4) and (8), the horizontal and vertical temperature gradients at the DFP are obtained as $\partial T_i/\partial x = \rho_s L_f u_p/(k_l - k_s)$, and $\partial T_i/\partial y = 0$, respectively. Thus, the temperature linearly increases in the x direction, with no gradient in the y direction and no change in slope at the interface. A positive horizontal gradient implies that the only way this configuration can exist is if the liquid is supercooled in front of the DFP, which is in favor of step nucleation at this point. However, when the pulling speed (u_p) is large or $k_l \approx k_s$, the amount of supercooling increases substantially, which increases the chance of unstable and dendritic growth at the DFP.

For materials like YAG with $k_l < k_s$, the temperature gradients are infinite at the DFP and their sign is not predictable because the sign and value of G_1 is unknown. This and the above discussions indicate that the behavior of YAG would be very different than that of silicon in a HRG growth experiment. As far as we know, however, no HRG experiments with YAG have been performed so it is unclear what implications these differences would have on the interface configuration in such an experiment.

4.3. Zigzag Configurations

A double facet formation can also occur in different configurations or boundary conditions. For example, faceted growth can lead to a zigzag formation with no free surface contact [18, 32]. In this case the leading points (LP) of the connected double facets (leading in the liquid) correspond to a DFP and the trailing points (TP) are similar to a TJP, except with $q_l = q_s = 0$. An example of a zigzag formation is shown in Fig. 5. Note that the facets here are again assumed to be symmetric with an adiabatic boundary condition crossing both the LP and TP points.

Referring to Eq. (6) and (8), the general formulation for the tangential and normal temperature gradients of a zigzag formation are

$$\begin{aligned}\left(\frac{\partial T_i}{\partial x^*}\right)_{\mathrm{LP\&TP}} &= -\frac{\rho_s L_f u_p}{k_l - k_s}\cos(\theta_l) + G_1 r^{\lambda_1 - 1},\\ \left(\frac{\partial T_i}{\partial y^*}\right)_{\mathrm{LP\&TP}} &= -\frac{\rho_s L_f u_p}{k_l - k_s}\sin(\theta_l) + \lambda_1 G_1 \tan(\lambda_1 \theta_i) r^{\lambda_1 - 1},\end{aligned} \tag{9}$$

where subscript i refers to either the liquid or solid domains. Whether each point has infinite temperature gradients or not, depends on the value of λ_1 that is obtained from Fig. 3 or Fig. 4 as a function of the thermal conductivities of the material and the angles of the liquid and solid interfaces. If the facets are aligned with the {111} faces such that the liquid interface angle at each point is $\theta_{l,\mathrm{LP}} \approx \pi - \theta_f$ and $\theta_{l,\mathrm{TP}} \approx -\theta_f$, the temperature gradients approach infinity at the TP and are finite at the LP for materials with $k_l > k_s$, such as silicon. Because

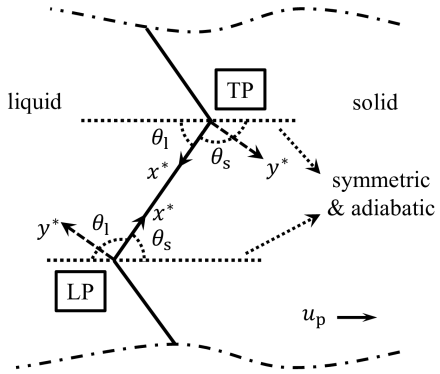

Figure 5: Schematic of a zigzag double facet formation with the description of the coordinate systems and the angles at the leading point (LP) and the trailing point (TP).

the tangential temperature gradient will be positive at the LP, it will likely be a nucleation site. In materials with $k_l < k_s$, such as YAG, the gradients are finite at the TP and infinite at the LP. For this case it is difficult to say whether the LP could be the step source or not.

5. Temperature Variations and Solidification Kinetics

As previously discussed, the rate of crystal growth and the solidification kinetics of a faceted configuration are a function of the local temperature variation. To analyze the crystal growth in a double facet formation, a solidification kinetics model is required. In this study, the kinetic model proposed by Weinstein and Brandon [14] is used, in which the temperature at each point on the solidification interface, T_I, is expressed as a function of the kinetic coefficient and the normal interface growth rate, such that $T_I = T_m + \Delta T_I = T_m + K(\alpha, \Delta T_I) u_{I,g,n}$, where T_m is the equilibrium melting point of the crystal. Note that $u_{I,g,n} = -u_p \sin(\theta_s)$ along the facet in the vicinity of both the TJP and DFP (see Fig. 2), because the interface is stationary and the growth rate must balance the rate of pulled material.

The kinetic coefficient is a function of the misalignment angle and interface supercooling, depending on the type of solidification that is likely to happen. Known mechanisms of step generation are either 2D nucleation on a facet or at a dislocation. For a single facet, the kinetic coefficients of $K_{2D} = K_{2Dn} \exp(A_{2Dn}/|\Delta T_I|)$ and $K_{dis} = K_{DG}/\Delta T_I$ are proposed for 2D nucleation and dislocation, respectively, where K_{2Dn}, A_{2Dn}, and K_{DG} are constants. In either formulation, the temperature at the step source can be implicitly obtained. However, it should be noted that no validated kinetic expression has been obtained for facet intersection points such as the DFP.

If the misalignment angle is small in the vicinity of the nucleation points, step propagation occurs on the facet with $K_{step} = K_{sn}/|\sin(\alpha)|$, where K_{sn} is constant. With the facet temperature estimations of Eq. (5) and (7) in the vicinity of the TJP and DFP, respectively, the facet misalignment angle can be estimated using this kinetic formulation if T_{TJP} and T_{DFP} are somehow obtained. Because the temperature is always finite in the vicinity of both points, the misalignment angle will be nonzero. However, taking the derivative of the step growth kinetic formulation shows that if the tangential temperature gradient (in the x^* direction) is infinite at either of the TJP or DFP, the rate of change of the misalignment angle will be also infinite. For example, for materials with $k_l > k_s$ such as silicon, α is finite and non-zero at the TJP but $\partial\alpha/\partial x^*$ is infinite, which could lead to curvature effects at this point.

6. Validation of the Theoretical Model

To validate the theoretical formulations, a global solution is obtained of a problem containing a DFP and a TJP, with an HRG-like configuration with a cooling heat flux at the free surfaces and silicon as the solidified material. The solution is obtained numerically and compared with the theoretical predictions, as described herein.

6.1. Numerical Analysis

An *hp*-finite element numerical formulation is used that accounts for convective liquid flow, conductive and convective heat transfer, and solidification kinetics. The formulation benefits from high-order approximation polynomials and a moving and adapting triangular arbitrary Lagrangian-Eulerian (ALE) mesh for tracking the solid-liquid interface position and resolving sharp gradients. The discretiziations are 5^{th} order accurate in space and 3^{rd} order accurate in time. The system of spatial and temporal equations in this method are solved using an A-stable diagonally implicit Runge-Kutta scheme. The interested reader is referred to reference [33] for more details.

To be consistent with the theoretical analysis, the numerical simulation assumes there is a symmetry plane parallel to the free surface and passing through the DFP at a depth of t_{DFP}. Figure 6 displays a sample of the numerical domain with the initial mesh in the liquid (Ω_l) and solid (Ω_s) domains and the specified flow and thermal boundary conditions on the domain boundaries. The domains are non-dimensionalized by $d = 100\,[\mu\text{m}]$, which is on the order of twice the DFP depth, t_{DFP}, observed in the experiments (see Fig. 1(c)).

The bottom boundaries (symmetry and adiabatic plane) and the top boundaries (free surface) of both domains have Neumann boundary conditions. The bottom boundaries have zero stress and zero heat flux. The top boundaries have zero stress but a prescribed heat flux, resembling convective heat flux by a cooling jet positioned at $x = 0$ plus radiative heat flux from the free surfaces to the ambient. The heat flux distribution is prescribed by [8]

$$q(x) = q_{c,peak} \exp\left(-(x/w)^2 \ln 2\right) + \varepsilon_i \sigma_b \left(T_s^4(x) - T_c^4\right), \tag{10}$$

where $q_{c,peak}$ is the peak convective heat flux at $x = 0$, w is the jet width, ε_i is the emissivity of the liquid or solid

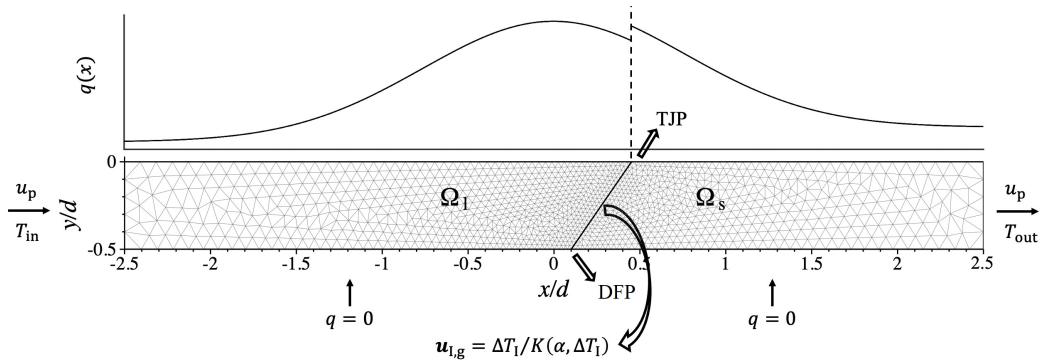

Figure 6: A sample of liquid and solid domains and meshes used for the numerical simulation with the specified flow and thermal boundary conditions and the solidification kinetic formulation at the liquid-solid interface.

silicon, σ_b is the Stefan-Boltzmann constant, $T_s(x)$ is the temperature at each axial position on the free surface, and T_c is the ambient temperature. Both domains are extended by $2.5d$ from the cooling jet center ($x = 0$) such that the streamwise variations of the heat flux diminish at the inlet (x_{in}) and outlet (x_{out}) of the domains. The liquid inlet and solid outlet have Dirichlet boundary conditions, with the temperatures fixed at $T_{in} > T_m$ and $T_{out} < T_m$, respectively, and the inlet velocity is fixed at the pulling speed, u_p.

At the liquid-solid interface, the solidification kinetic model of §5 is used, such that the interface velocity at each time-step is obtained from the local interface supercooling and the appropriate kinetic coefficient, $\boldsymbol{u}_{l,g} = \Delta T_l / K(\alpha, \Delta T_l)$. Although the type of kinetics at the DFP is unknown, it is assumed that 2D nucleation occurs at the DFP with the kinetic formulation provided in §5. Using this formulation, T_{DFP} is obtained during the simulation. The interface is initially positioned downstream (to the right) of the cooling jet center to create a supercooled region in the liquid by the cooling heat flux. The converged steady-state position of the interface relative to the heat flux profile will be a function of the balance between the generated heat at the interface (a function of the pulling speed) and the removed heat.

6.2. Theoretical Vs. Numerical

The parameters for the particular studied case of a double facet formation are listed in Table 1.

The converged steady-state temperature solution for this problem is shown in Fig. 7, where the temperature contours (isotherms) are visible as dashed lines. Both the DFP and TJP are positioned upstream (left) of the cooling jet center at $x_{DFP}/d = -0.44$ and $x_{TJP}/d = -0.08$. The minimum temperature occurs in the solid downstream of the TJP and the cooling jet center at $x/d = +0.70$ with $T_{min} = 1674.4\,[\mathrm{K}]$. At the TJP, the liquid and solid heat fluxes are $q_l = 116\,[\mathrm{W/cm^2}]$ and $q_s = 134\,[\mathrm{W/cm^2}]$. These values will be later used in the theoretical estimation of temperature gradients at the interface. The temperature contours make zero normal gradient at the symmetry boundary because of the adiabatic boundary condition. A supercooled region exists in front of the entire interface in the liquid region with $|\Delta T| \approx$ 4-7 [K] ($T_m = 1685\,[\mathrm{K}]$). This liquid supercooling is necessary to initiation the growth of steps on the facet. Note that the melting point isotherm is far upstream of the facet.

Table 1: Parameters for the studied case for theoretical and numerical comparison [14]

Description	**Variable**	**Value**	**[Units]**
DFP depth	t_{DFP}	50	[μm]
pulling speed	u_p	0.4	[mm/s]
solid/liquid density	ρ	2530	[kg/m^3]
solid/liquid spec. heat	c	1000	[J/kg K]
solid conductivity	k_s	22	[W/m K]
liquid conductivity	k_l	64	[W/m K]
equi. melting temp.	T_m	1685	[K]
inlet temp.	T_{in}	1687	[K]
outlet temp.	T_{out}	1683	[K]
peak conv. heat flux	$q_{c,peak}$	100	[W/cm^2]
cooling jet width	w	100	[μm]
solid emissivity	ε_s	0.6	-
liquid emissivity	ε_l	0.2	-
2D nucl. kinetic const.	K_{2Dn}	$1/(1.5 \times 10^{10})$	[K/(m/s)]
2D nucl. kinetic const.	A_{2Dn}	140	[K]
step kinetic const.	K_{sn}	1/0.63	[K/(m/s)]

The variation of temperature along the interface is shown in Fig. 8(a), where temperature at the DFP is equal to $T_{DFP} = 1680.7\,[\mathrm{K}]$. Although it is difficult to see in Fig. 8(a), the temperature slightly increases by moving away from the DFP in the x^* direction, as

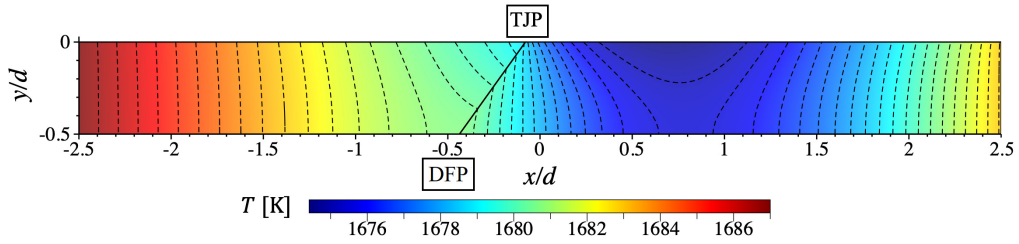

Figure 7: Numerical solution showing the temperature contours in the liquid and solid domains in a region close to the top facet of a double facet formation for the studied case of Table 1.

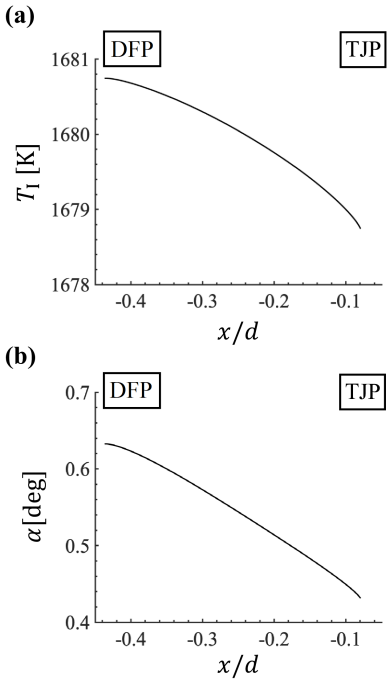

Figure 8: Numerical solution for the studied case of Table 1 showing the (a) temperature distribution along the facet, and (b) variation of the misalignment angle along the facet.

predicted by Eq. (7). However, the temperature then decreases by moving toward the TJP, where the temperature is $T_{\mathrm{TJP}} = 1678.8\,[\mathrm{K}]$. This can be explained by the singular tangential temperature gradient at the TJP predicted by Eq. (6) for silicon, as will be observed later. The facet misalignment angle in Fig. 8(b) has a similar variation. At the DFP, the misalignment angle starts from $\alpha_{\mathrm{DFP}} = 0.63\,[\mathrm{deg}]$, slightly increases, and then sharply drops to $\alpha_{\mathrm{TJP}} = 0.43\,[\mathrm{deg}]$ at the TJP because of the decreasing facet temperature. Because the misalignment angle over the entire facet is smaller than the onset of transition to roughened growth at $\alpha_{\mathrm{trans}} = \sin^{-1}(K_{\mathrm{sn}}/K_{\mathrm{rough}}) \approx 11\,[\mathrm{deg}]$, the mechanism for crystal formation on the entire facet is step growth.

The numerical tangential (x^*) and normal (y^*) facet temperature gradients in the vicinity of the DFP are derived from the solution in Fig. 8 and are shown in Fig. 9(a) in the DFP coordinate system (see Fig. 2). It can be observed that the tangential temperature gradient (solid black line) is positive is a small region close to the DFP, $x^*/d < 0.003$, yielding a temperature increase of about 0.004 [K] in this region. This explains why this temperature increase is not clearly visible in Fig. 8(a).

The theoretical estimations of the temperature gradients at the DFP from Eq. (8) are also shown as symbols in Fig. 9(a), where $A_{\mathrm{DFP}} = 24.9\,[\mathrm{K/mm}]$ (black circle) and $B_{\mathrm{DFP}} = -35.5\,[\mathrm{K/mm}]$ (blue square) are the theoretical tangential and normal gradients at the DFP, respectively, which are equal for both the liquid and solid domains. Evaluating the numerical gradients at the DFP location in Fig. 9(a) results in $\partial T_{\mathrm{l}}/\partial x^* = \partial T_{\mathrm{s}}/\partial x^* = 11.6\,[\mathrm{K/mm}]$, $\partial T_{\mathrm{l}}/\partial y^* = -23.4\,[\mathrm{K/mm}]$, and $\partial T_{\mathrm{s}}/\partial y^* = -7.86\,[\mathrm{K/mm}]$. It can be observed that the numerical temperature gradients are finite at the DFP, as predicted by Eq. (8) for silicon, and approach the values predicted by the analysis. Although the numerical solid and liquid normal gradients have different values, they both converge to the theoretical value by performing a grid refinement procedure that will be shown later.

The numerical facet temperature gradients in the vicinity of the TJP are shown in Fig. 9(b). At this point, the temperature gradients cannot be theoretically estimated due to the unknown G_1 value in the homogeneous solution (see §4.1). It can be observed in Fig. 9(b) that the numerical temperature gradients, displayed as lines, are completely different from the theoretical prediction for the non-homogeneous part of the gradients in Eq. (6), A_{TJP}, $B_{\mathrm{l,TJP}}$, and $B_{\mathrm{s,TJP}}$, which are shown as symbols. This means that the singular homogeneous part of the temperature gradients dominate the gradients at

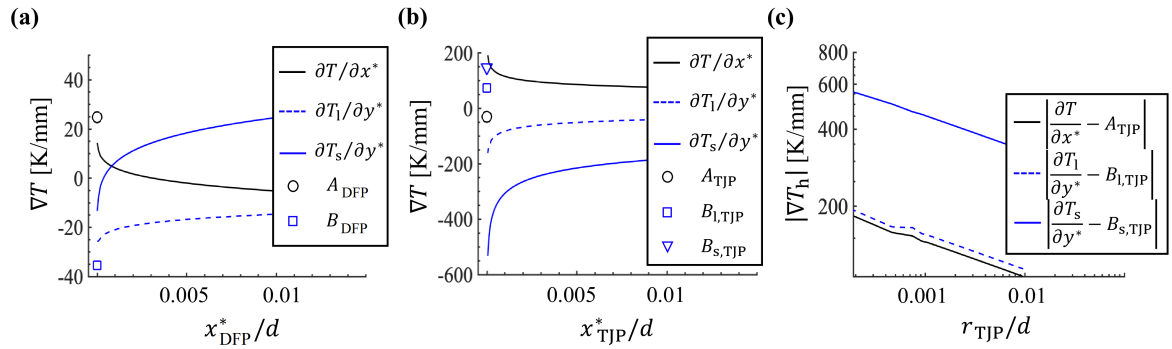

Figure 9: Comparison of numerical and theoretical temperature gradients, (a) temperature gradients in the vicinity of the DFP, (b) temperature gradients in the vicinity of the TJP, and (c) homogeneous part of the temperature gradients on a logarithmic scale in the vicinity of the TJP.

the TJP, which is consistent with the theoretical analysis. Because the tangential temperature gradient (solid black line) is positive and the normal temperature gradients (blue lines) are negative at the TJP, the coefficient G_1 in Eq. (6) should be positive in the specific configuration studied here.

The first radial power of the homogeneous solution at the TJP, λ_1, can be estimated from the homogeneous part of the numerical temperature gradients and be compared with the theoretical prediction from Eq. (2). This can be done by subtracting the theoretical non-homogeneous temperature gradients at the TJP ($A_{\mathrm{i,TJP}}$ and $B_{\mathrm{i,TJP}}$) from the numerical temperature gradients (∇T). By plotting the resulting numerical homogeneous temperature gradients, ∇T_{h}, versus the radius from the TJP on a logarithmic scale, λ_1 should be equal to the slope of the variations (see Eq. (6)). These plots are shown in Fig. 9(c), where the evaluated numerical slopes are $\lambda_{1,\mathrm{x^*}} = 0.8632$, $\lambda_{1,\mathrm{y^*,l}} = 0.8657$, and $\lambda_{1,\mathrm{y^*,s}} = 0.8647$, for tangential, normal in the liquid, and normal in the solid gradients, respectively. It is evident that these values are extremely close to the theoretical prediction of $\lambda_1 = 0.8606$.

For a more accurate comparison between the theoretical and numerical results, the mesh is refined twice to increase the grid resolution at the DFP and TJP. The evaluated numerical results are shown in Table 2 in comparison with the theoretical estimations. In addition, the numerical values in the limit that the grid element size approaches zero are obtained using a Richardson extrapolation technique [34] and reported in Table 2, along with the numerical convergence rate of each parameter. It can be observed that the extrapolated temperature gradients at the DFP and the λ_1 values at the TJP approach the theoretical predictions. The normal liquid and solid temperature gradients at the DFP are also closer after extrapolation. This confirms that the theoretical formulations are good estimates of the behavior of a double facet formation in close proximity of its two end points, the DFP and TJP.

As a final note, a positive G_1 in Eq. (6) means that the horizontal temperature gradient, $\partial T/\partial x$, is infinitely negative (see Eq. (4)), resulting in a large Marangoni-induced flow toward the TJP with the minimum liquid free-surface temperature at the TJP. This behavior could be observed experimentally by visualizing the liquid surface velocities with marker particles. Note that surface tension variation has not been included in the numerical simulation. It has been shown in prior studies that the TJP position moves downstream as the pulling speed is increased [8]. At large pulling speeds, the minimum temperature occurs in the liquid and there is a chance that the facet temperature increases toward the TJP, making G_1 positive. With a positive G_1, the horizontal temperature gradient will be infinitely positive at the TJP, resulting in a large Marangoni-induced flow from the TJP toward the minimum temperature location. While this condition decreases the chance of crystal contamination, it increases the risk of dendritic growth at the TJP due to a large supercooled liquid region in front of it.

7. Conclusions

The special case of a double facet formation in solidification processes was investigated in this paper, including different possible configurations and crystallized materials. The physical behavior of facets and their intersection or end points were analyzed theoretically to explore the temperature fields and solidification kinetics at these points. It was observed that the behavior of facet end points is primarily a function of the

Table 2: Results of mesh refinement performed on the studied case of Table 1.

Description	Variable	Base case	1st Refine.	2nd Refine.	Extrap. (Conv. Rate)	Analytical	[Units]
grid size	N_e	19k	74k	298k	–	–	elements
min. element size	$\Delta x_{min}/d$	5.6×10^{-5}	2.8×10^{-5}	1.4×10^{-5}	–	–	–
DFP tangential temp. gradient	$\left(\frac{\partial T_i}{\partial x^*}\right)_{DFP}$	−11.6	−13.1	−14.3	−19.1 (0.32)	−24.9	[K/mm]
DFP liq. normal temp. gradient	$\left(\frac{\partial T_l}{\partial y^*}\right)_{DFP}$	23.4	24.7	25.8	31.9 (0.24)	35.5	[K/mm]
DFP sol. normal temp. gradient	$\left(\frac{\partial T_s}{\partial y^*}\right)_{DFP}$	7.86	10.7	13.3	41.5 (0.13)	35.5	[K/mm]
TJP tangential 1st radial power	λ_{1,x^*}	0.8632	0.8621	0.8613	0.8592 (0.46)	0.8606	–
TJP liq. normal 1st radial power	$\lambda_{1,y^*,l}$	0.8657	0.8637	0.8624	0.8617 (0.62)	0.8606	–
TJP sol. normal 1st radial power	$\lambda_{1,y^*,s}$	0.8647	0.8631	0.8620	0.8596 (0.54)	0.8606	–

material thermal conductivities in the liquid and solid forms and the angles at which the facets intersect each other or the free surfaces. For materials with $k_l > k_s$, such as silicon, a double facet formation with a {111} crystallographic orientation at its end points was shown to have theoretically finite temperature gradients at the double facet point or the leading point in the case of a zigzag formation, and infinite temperature gradients at the other end, the triple junction point or the trailing point. The situation was shown to be reversed for a material with $k_l < k_s$, such as yttrium aluminum garnet. Existence of infinite or large temperature gradients at any of the facet end points can cause large supercooled regions and Marangoni-induced flows in proximity of the points. Numerical simulation of an example case with a double facet formation showed that the theoretical formulations can successfully estimate the temperature variations in the vicinity of the facet end points, demonstrating their ability in predicting the behavior of a double facet formation in different configurations and conditions. Work in needed to experimentally verify these predictions and also to understand the nucleation process that is assumed to occur at a double facet point.

Acknowledgments

This material is based upon work supported by the National Science Foundation (NSF) under Grant No. 1762802.

References

[1] O. Weinstein, W. Miller, Three-dimensional calculations of facets during Czochralski crystal growth, Journal of Crystal Growth 312 (7) (2010) 989–996.

[2] A. Witt, M. Lichtensteiger, H. Gatos, Application of Interface Demarcation to the Study of Facet Growth and Segregation: Germanium, J. Electrochem. Soc. (USA) 121 (6) (1974/06/) 787 – 90, ISSN 0013-4651.

[3] T. Duffar (Ed.), Crystal Growth Processes Based on Capillarity: Czochralski, Floating Zone, Shaping, and Crucible Techniques, John Wiley & Sons, 2010.

[4] L. Stockmeier, L. Lehmann, A. Miller, C. Reimann, J. Friedrich, Dislocation formation in heavily As-doped Czochralski grown silicon, Crystal Research and Technology 52 (8) (2017) 1600373, doi:10.1002/crat.201600373.

[5] A. Krauze, J. Virbulis, S. Zitzelsberger, G. Ratnieks, 3D modeling of growth ridge and edge facet formation in (100) floating zone silicon crystal growth process, Journal of Crystal Growth 520 (2019) 68–71, ISSN 0022-0248, doi: 10.1016/j.jcrysgro.2019.04.030.

[6] A. S. Greenlee, Towards the Development of a Horizontal Ribbon Growth Process to Produce Thin, Monocrystalline Silicon Sheets via the Stabilization of the (111) Plane in Undercooled Melts, Ph.D. thesis, Massachusetts Institute of Technology, 2015.

[7] B. T. Helenbrook, Solidification along a wall or free surface with heat removal, Journal of Crystal Growth 418 (2015) 79 – 85, ISSN 0022-0248, doi:10.1016/j.jcrysgro.2015.02.028.

[8] A. Pirnia, B. T. Helenbrook, Analysis of faceted solidification in the horizontal ribbon growth crystallization process, Journal of Crystal Growth 555 (2021) 125958, ISSN 0022-0248, doi: 10.1016/j.jcrysgro.2020.125958.

[9] C. Lan, C. Chen, Dynamic three-dimensional simulation of facet formation and segregation in Bridgman crystal growth, Journal of Crystal Growth 303 (1) (2007) 287–296.

[10] K. Jackson, Crystal growth kinetics, Materials Science and Engineering 65 (1) (1984) 7–13, ISSN 0025-5416, doi: 10.1016/0025-5416(84)90194-0, solidification Microstructure: 30 Years after Constitutional Supercooling.

[11] A. Trainor, B. Bartlett, A Possible Mechanism of Crystal Growth from the Melt and Its Application to the Problem of Anomalous Segregation at Crystal Facets, Solid-State Electronics 2 (2) (1961) 106–114.

[12] O. Weinstein, S. Brandon, Dynamics of partially faceted melt/crystal interfaces II: multiple step–source calculations,

Journal of Crystal Growth 270 (1) (2004) 232–249.
[13] Y. Liu, A. Virozub, S. Brandon, Facetting during Directional Growth of Oxides from the Melt: Coupling between Thermal Fields, Kinetics and Melt/Crystal Interface Shapes, Journal of Crystal Growth 205 (3) (1999) 333–353.
[14] O. Weinstein, S. Brandon, Dynamics of partially faceted melt/crystal interfaces I: computational approach and single step–source calculations, Journal of Crystal Growth 268 (1) (2004) 299–319.
[15] K. Beatty, K. Jackson, Monte Carlo Modeling of Silicon Crystal Growth, Journal of Crystal Growth 211 (1) (2000) 13–17.
[16] K. Fujiwara, K. Maeda, N. Usami, K. Nakajima, Growth Mechanism of Si-Faceted Dendrites, Physical review letters 101 (5) (2008) 055503.
[17] J. Pohl, M. Müller, A. Seidl, K. Albe, Formation of Parallel (1,1,1) Twin Boundaries in Silicon Growth from the Melt Explained by Molecular Dynamics Simulations, Journal of Crystal Growth 312 (8) (2010) 1411 – 1415, ISSN 0022-0248, doi: 10.1016/j.jcrysgro.2009.09.043.
[18] G. Chen, H. Lin, C. Lan, Phase-Field Modeling of Twin-Related Faceted Dendrite Growth of Silicon, Acta Materialia 115 (2016) 324–332.
[19] V. Oliveira, B. Marie, C. Cayron, M. Marinova, M. Tsoutsouva, H. Sio, T. Lafford, J. Baruchel, G. Audoit, A. Grenier, T. Tran Thi, D. Camel, Formation mechanism and properties of twinned structures in (111) seeded directionally solidified solar grade silicon, Acta Materialia 121 (2016) 24–36, ISSN 1359-6454, doi: 10.1016/j.actamat.2016.08.063.
[20] V. Stamelou, M. Tsoutsouva, T. Riberi-Béridot, G. Reinhart, G. Regula, J. Baruchel, N. Mangelinck-Noël, 111 facet growth laws and grain competition during silicon crystallization, Journal of Crystal Growth 479 (2017) 1–8, ISSN 0022-0248, doi: 10.1016/j.jcrysgro.2017.09.013.
[21] N. Dey, J. Sekhar, Interface configurations during the directional growth of Salol—I. Morphology, Acta Metallurgica et Materialia 41 (2) (1993) 409–424, ISSN 0956-7151, doi: 10.1016/0956-7151(93)90071-Y.
[22] K. Kuniyoshi, K. Ozono, M. Ikeda, T. Suzuki, S. Gyoon Kim, W. Tae Kim, Faceted dendrite growth of silicon from undercooled melt of Si-Ni alloy, Science and Technology of Advanced Materials 7 (6) (2006) 595 – 600, ISSN 14686996, dendritic growth;Phase field model;Undercooling solidification;.
[23] X. Yang, K. Fujiwara, R. Gotoh, K. Maeda, J. Nozawa, H. Koizumi, S. Uda, Effect of Twin Spacing on the Growth Velocity of Si Faceted Dendrites, Applied Physics Letters 97 (17) (2010) 2104.
[24] L. Stockmeier, C. Kranert, G. Raming, A. Miller, C. Reimann, P. Rudolph, J. Friedrich, Edge facet dynamics during the growth of heavily doped n-type silicon by the Czochralski-method, Journal of Crystal Growth 491 (2018) 57–65, ISSN 0022-0248, doi:10.1016/j.jcrysgro.2018.03.028.
[25] C. Kranert, G. Raming, A. Miller, C. Reimann, J. Friedrich, Facet growth and geometry of the growth ridge during dynamic Czochralski processes, Journal of Crystal Growth (2021) 126174ISSN 0022-0248, doi:10.1016/j.jcrysgro.2021.126174.
[26] P. Kellerman, B. Kernan, B. T. Helenbrook, D. Sun, F. Sinclair, F. Carlson, Floating Silicon Method single crystal ribbon – observations and proposed limit cycle theory, Journal of Crystal Growth 451 (2016) 174 – 180, ISSN 0022-0248, doi: 10.1016/j.jcrysgro.2016.07.012.
[27] B. T. Helenbrook, N. S. Barlow, Spatial–temporal stability analysis of faceted growth with application to horizontal ribbon growth, Journal of Crystal Growth 454 (2016) 35 – 44, ISSN 0022-0248, doi:10.1016/j.jcrysgro.2016.08.052.
[28] M. Mito, T. Tsukada, M. Hozawa, C. Yokoyama, Y.-R. Li, N. Imaishi, Sensitivity Analyses of the Thermophysical Properties of Silicon Melt and Crystal, Measurement Science and Technology 16 (2) (2005) 457.
[29] N. Eustathopoulos, B. Drevet, Surface Tension of Liquid Silicon: High or Low Value?, Journal of Crystal Growth 371 (2013) 77–83.
[30] H. Minakuchi, et al., A Grid Refinement Study of Half-Zone Configuration of the Floating Zone Growth System, Journal of Advanced Research in Physics 3 (1).
[31] P. Daggolu, A. Yeckel, C. E. Bleil, J. J. Derby, Thermal-Capillary Analysis of the Horizontal Ribbon Growth of Silicon Crystals, Journal of Crystal Growth 355 (1) (2012) 129–139.
[32] K. Fujiwara, M. Tokairin, W. Pan, H. Koizumi, J. Nozawa, S. Uda, Instability of Crystal/Melt Interface Including Twin Boundaries of Silicon, Applied Physics Letters 104 (18) (2014) 182110.
[33] B. Helenbrook, J. Hrdina, High-order adaptive arbitrary-Lagrangian–Eulerian (ALE) simulations of solidification, Computers and Fluids 167 (2018) 40 – 50, ISSN 0045-7930, doi: 10.1016/j.compfluid.2018.02.028.
[34] . (July 22, Procedure for Estimation and Reporting of Uncertainty Due to Discretization in CFD Applications, Journal of Fluids Engineering 130 (7), ISSN 0098-2202, doi: 10.1115/1.2960953, 078001.